PCCP

Accepted Manuscript

ROYAL SOCIETY OF CHEMISTRY

www.rsc.org/pccp

Origin of distinct structural symmetry of the neopentane cation in the ground electronic state compared to the methane cation

T. Mondal*

Department of Chemistry, Birla Institute of Technology & Science, Pilani - K.K. Birla Goa Campus, Goa 403 726, India

Abstract

An *ab initio* quantum dynamics study has been performed to explore the distinct structural symmetry of $C(CH_3)_4^+$ in the ground electronic state when compare it with CH_4^+. Additionally, the underlying details of the highly diffuse and complex vibronic structure of the first photoelectron band of $C(CH_3)_4$ have been investigated. Associated potential energy surfaces over the two-dimensional space of nuclear coordinates, subject to the $T_2 \otimes (e + t_2)$ Jahn-Teller effect, are established from extensive electronic structure calculations and (then) the nuclear dynamics calculations are done on them via wave packet propagation including the nonadiabatic coupling of the three electronic sheets. The theoretical results are in good agreement with experimental observations. The JT stabilization energies due to $T_2 \otimes e$, $T_2 \otimes t_2$ and $T_2 \otimes (e + t_2)$ distortions in the $\widetilde{X}\,^2T_2$ electronic manifold of $C(CH_3)_4^+$ illustrate that the highest stabilization occurs through the $T_2 \otimes t_2$-JT distortion (in the ground state of $C(CH_3)_4^+$). However, CH_4^+ gains such a maximum stabilization due to $T_2 \otimes (e + t_2)$-JT distortion. From this novel result and applying the epikernel principle, we proposes that the structural evolution of $C(CH_3)_4^+$ from T_d to C_{3v} minimum energy configurations occurs via JT active vibrations of t_2 symmetry, whereas CH_4^+ rearranges to the C_{2v} structure through a combination of JT active e and t_2 bending vibrations.

*Electronic address: tanmoym@goa.bits-pilani.ac.in

I. INTRODUCTION

Degeneracies of electronic potential energy surfaces (PESs) are ubiquitous in molecular systems. One of the reasons for such degeneracy is the high symmetry of the molecular configurations. The Jahn-Teller (JT) effect is an unique vibronic coupling phenomena in chemical physics where the above mentioned degeneracies in highly symmetric nonlinear molecular configurations are lifted via symmetry-lowering distortions[1–9] and thus playing a crucial role in the structure and dynamics of such molecular systems. The effect arises due to the coupling involving vibrational modes and degenerate electronic states at highly symmetrical nuclear configurations. Thus, the adiabatic or Born-Oppenheimer (BO) approximation breaks down and a concurrent treatment of electronic and nuclear motions is essential under such conditions. The simplest possibility arises for a molecule with a twofold degenerate electronic state of E symmetry at C_{3v} geometry. The symmetry selection rule suggests that such a twofold degenerate electronic state would undergo JT splitting in first-order when distorted along the degenerate mode of e symmetry (note that the symmetry of the electronic and nuclear degrees of freedom are designated by the upper and lower case symbols, respectively). This leads to the well known $E \otimes e$ JT effect.[1–9] The next higher analogue present in molecules with threefold degenerate electronic state where the degeneracy of the electronic PESs at T_d geometry is splitted by the nuclear coordinates of e and t_2 symmetry, yielding the $T_2 \otimes (e + t_2)$ JT effect. [5, 10–16]

Methane radical cation (CH_4^+) is the lowest alkane radical cation possessing a threefold degenerate electronic ground state ($\widetilde{X}\,^2T_2$), and thus representing the prototype system for the $T_2 \otimes (e + t_2)$ JT problem. Earlier investigations revealed that the minimum energy structure of the CH_4^+ belongs to a distorted geometry (compared to the T_d geometry of methane) with C_{2v} symmetry,[17, 18] due to JT effect. Experimental evidence for the above C_{2v} geometry of CH_4^+ was observed by Knight *et al.* [19, 20] via electron spin resonance (ESR) spectroscopy experiments in a neon matrix and by Vager *et al.* [21] from Coulomb explosion experiments. This characterization of C_{2v} structure was also fully confirmed by high resolution optical spectra observed from pulsed-field-ionization zero-energy-kinetic-energy spectroscopy.[22, 23] Recently Domcke and coworkers reported two diabatic PESs for the $\widetilde{X}\,^2T_2$ electronic manifold of CH_4^+, subject to the $T_2 \otimes (t_2 + t_2)$[24] and $T_2 2 \otimes e$[25] JT effect, in terms of a high-order polynomial expansion in symmetry-adapted nuclear displacement

coordinates with respect to a reference T_d geometry. Subsequently they have constructed a three-sheeted nine-dimensional adiabatic PES surface of the $\widetilde{X}\,^2T_2$ electronic ground state of CH_4^+ via a linear optimization procedure.[26] Very recently we have simulated the first photoelectron band of CH_4^+ via an *ab initio* quantum dynamics study and settled down the longstanding ambiguity over the assignment of dominant vibrational progressions underlying this photoelectron band.[27, 28] Furthermore, we have calculated the ratio of square autocorrelation functions between the CH_4^+ on its threefold degenerate ground electronic state and its deuteriated isotopomer, and established that the distortion of methane cation from T_d to C_{2v} configuration occurs in $\sim$1.85 fs.[29] Such an evolution is predicted to begin through activation of a_1 and e modes. While the former retains the original T_d symmetry of the cation, the JT active e mode conducts it to a D_{2d} structure. At $\sim$1.85 fs, the intermediate D_{2d} structure is further rearranged to a local C_{2v} minimum via JT active bending vibrations of t_2 symmetry.[30]

Geometrical structures of methylated methane radical cations across the five members of the series $CH_{4-n}(CH_3)_n^+$ where $n = 0, 1, 2, 3, 4$ have also been probed by ESR spectroscopy.[31–34] The highly symmetric methane and neopentane radical cations possesses threefold degenerate electronic ground state and exhibit $T_2 \otimes (e + t_2)$ type JT problem, and for lower symmetric ethane and isobutane radical cations this threefold degenerate electronic state splits into a twofold degenerate and a nondegenerate electronic state. Thus, the latter two radical cations show both JT and pseudo-Jahn-Teller (PJT) activity within this electronic manifold. However, for nonsymmetric propane radical cation, the parent threefold electronic degeneracy is lifted to three nondegenerate electronic states and thereby, the JT activity vanishes for this radical cation. It is interesting to note that although both methane and neopentane have a T_d equilibrium structure, and ionization of an electron from their highest occupied molecular orbitals (HOMO) yields both CH_4^+ and $C(CH_3)_4^+$ in their ground state $\widetilde{X}\,^2T_2$, the JT effect distorts the cations differently. While six equivalent C_{2v} ($^2B_1$) minimum energy structures are found in case of CH_4^+, the $C(CH_3)_4^+$ rearranges to four equivalent C_{3v} ($^2A_1$) minimum energy configurations. Such a C_{3v} geometrical structure of ground state $C(CH_3)_4^+$ was confirmed by ESR spectroscopy experiment. [32] The observed four-line spectrum arising from the hyperfine coupling with three equivalent protons clearly indicates the C_{3v} geometry of the cation. This is further suggested by the INDO calculations where the total energy of $C(CH_3)_4^+$ is decreased by a distortion from T_d to C_{3v}. [32] There-

fore, the goal of the present article is to explore the underlying mechanism for the above distinct structural distortion in ground state $C(CH_3)_4^+$ compared to CH_4^+. In particular our target is to nailed down the vibrational modes responsible for such anomolus structural rearrangement in $C(CH_3)_4^+$.

The He I photoelectron spectrum of $C(CH_3)_4$, recorded by several groups, revealed a highly diffuse and overlapping vibronic structure of the first photoelectron band of $C(CH_3)_4$.[35–38] The first photoelectron band originates due to ionization of an electron from the triply degenerate HOMO, $4t_2$. Therefore, the JT interactions within the threefold degenerate ground electronic manifold ($\widetilde{X}\,^2T_2$) of $C(CH_3)_4^+$ are expected to have profound impact on its nuclear dynamics. Additionally the low intensity of the partial photoelectron cross section for the $\widetilde{X}\,^2T_2$ state of $C(CH_3)_4^+$ as a function of the photoelectron kinetic energy in comparison with the next two higher electronic states observed in Constant Ionic State (CIS) experiments discard the possibility that the ionization out of HOMO is accompanied by any resonance phenomenon with other molecular orbitals. [38] These crucial issues are also addressed and examined in this article.

We focus therefore our attention in the present work to devise a theoretical model to examine the structureless first vibronic band and JT distortion dynamics of the $\widetilde{X}\,^2T_2$ electronic manifold of $C(CH_3)_4^+$. Recall that the electronic nonadiabatic coupling may have a pivotal role to achieve a satisfying interpretation of the highly overlapping and complex structure of the first photoelectron band of $C(CH_3)_4$. Thus, the three lowest adiabatic electronic states of the neopentane cation must be considered, including all relevant vibrational degrees of freedom. For this purpose a diabatic formalism will be employed, with the elements of the diabatic electronic Hamiltonian matrix being considered up to quadratic terms. They will be formed from all possible nontotally symmetric tensor convolutions involving up to quadratic combinations of the JT active vibrational modes, *i.e.*, a quadratic vibronic coupling (QVC) scheme. [6]

Ab initio electronic structure calculations are performed to derive the relevant coupling parameters of the vibronic Hamiltonian discussed in Section II. Since a time-independent matrix diagonalization approach to treat the nuclear dynamics on the three interacting electronic states in full dimensions of vibrational degrees of freedom is computationally unaffordable, the task will then be accomplished via a time-dependent wave packet (WP) propagation scheme using the multiconfiguration time-dependent Hartree (MCTDH) method. [39–43]

This is known to be very successful, particularly in treating the multistate and multimode vibronic coupling problems of large dimensionalities; [39–43] the details of the MCTDH method are well documented. [39–43] While the final results of this paper are obtained by this method, various calculations to assign the vibrational excitations towards the partial spectra in terms of a_1, e and t_2 vibrational modes have been carried out in reduced dimensionality via a matrix diagonalization approach [6] using the Lanczos algorithm. [44]. The diagonal elements of the resulting eigenvalue matrix give the energies of the vibronic levels and the relative intensities calculated from the squared leading components of the Lanczos eigenvectors. [45] Our results revealed that the large JT stabilization energy due to $T_2 \otimes t_2$ JT distortion yields $C(CH_3)_4^+$ at the C_{3v} minimum energy structure and the strong JT effect in the ground $\widetilde{X}\,^2T_2$ state primarily contributes to the highly diffuse vibronic structures of the first photoelectron band of $C(CH_3)_4$.

II. THEORETICAL FRAMEWORK AND COMPUTATIONAL DETAILS

A. Vibronic Hamiltonian

In the following, we construct a suitable model vibronic coupling Hamiltonian to simulate the nuclear dynamics underlying the first vibronic band of the ground ($\widetilde{X}\,^2T_2$) electronic state of $C(CH_3)_4^+$. The 45 vibrational degrees of freedom of neopentane decompose into the following irreducible representations (IREPs) of the T_d symmetry point group:

$$\Gamma = 3a_1(\nu_1 - \nu_3) + a_2(\nu_4) + 4e(\nu_5 - \nu_8) + 4t_1(\nu_9 - \nu_{12}) + 7t_2(\nu_{13} - \nu_{19}). \quad (1)$$

The symmetrized direct product of two T_2 representations in this point group yields

$$(T_2)^2 = A_1 + E + T_2. \quad (2)$$

Therefore, applying the elementary symmetry selection rule, $\Gamma_n \otimes \Gamma_Q \otimes \Gamma_m \supset A_1$, (with, Γ representing the IREPs; n, m denoting the electronic state index and Q defining the coordinate of the relevant vibrational mode) one finds that the $\widetilde{X}\,^2T_2$ electronic state would undergo JT splitting in first-order when distorted along doubly degenerate (e) or triply degenerate (t_2) vibrational modes. Whereas the totally symmetric (a_1) vibrational mode is

tuning-active within this electronic manifold and can not split the electronic degeneracy. [6] A diabatic electronic representation is employed to set up the Hamiltonian, and the coupling terms included in the potential energy via a Taylor series expansion of the electronic matrix elements in terms of dimensionless normal coordinates (*e.g.*, Q_i for vibrational mode ν_i) of the electronic ground state ($\widetilde{X}\,^1A_1$) of $C(CH_3)_4$. The normal coordinates (Q_i) actually refer to the displacements from the equilibrium configuration $\mathbf{Q}=\mathbf{0}$ of ground state $C(CH_3)_4$. The elements of the electronic matrix are considered up to second-order terms of all possible nontotally symmetric tensor convolutions that can be obtained from quadratic combinations involving the JT active e and t_2 vibrations.

The diabatic vibronic Hamiltonian, on the basis of dimensionless normal coordinates (Q_i) of the vibrational modes (ω_i), then assumes the form

$$\mathcal{H} = \mathcal{H}_0\mathbf{1_3} + \mathcal{W}. \tag{3}$$

Where $\mathcal{H}_0$=$\mathcal{T}_N + \mathcal{V}_0$, represents the unperturbed Hamiltonian of the electronic ground state of the neutral $C(CH_3)_4$ within a harmonic approximation of nuclear motion with,

$$\mathcal{T}_N = -\frac{1}{2}\sum_{i\,\in\,a_1,\,a_2}\omega_i\frac{\partial^2}{\partial Q_i^2} - \frac{1}{2}\sum_{i\,\in\,e}\omega_i\left(\frac{\partial^2}{\partial Q_{i\theta}^2}+\frac{\partial^2}{\partial Q_{i\epsilon}^2}\right) - \frac{1}{2}\sum_{i\,\in\,t_1,\,t_2}\omega_i\left(\frac{\partial^2}{\partial Q_{i\xi}^2}+\frac{\partial^2}{\partial Q_{i\eta}^2}+\frac{\partial^2}{\partial Q_{i\zeta}^2}\right) \tag{4}$$

and

$$\mathcal{V}_0 = \frac{1}{2}\sum_{i\,\in\,a_1,\,a_2}\omega_i Q_i^2 + \frac{1}{2}\sum_{i\,\in\,e}\omega_i\left(Q_{i\theta}^2+Q_{i\epsilon}^2\right) + \frac{1}{2}\sum_{i\,\in\,t_1,\,t_2}\omega_i\left(Q_{i\xi}^2+Q_{i\eta}^2+Q_{i\zeta}^2\right). \tag{5}$$

The change of electronic energy upon ionization is expressed by the electronic Hamiltonian matrix with $\mathcal{W}$ in Eq.(3) given by [11, 14–16]

$$\begin{aligned}\mathcal{W} =& (E_0 + \sum_{i\,\in\,a_1}\kappa_i Q_i)\mathbf{e}_\alpha + \sum_{i\,\in\,e}\lambda_i(Q_{i\theta}\mathbf{e}_\theta + Q_{i\epsilon}\mathbf{e}_\epsilon) + \sum_{i\,\in\,t_2}\mu_i\left(Q_{i\xi}\mathbf{t}_\xi + Q_{i\eta}\mathbf{t}_\eta + Q_{i\zeta}\mathbf{t}_\zeta\right)\\ &+\frac{1}{2}\left[\sum_{i\,\in\,a_1,\,a_2}\gamma_i Q_i^2 + \sum_{i\,\in\,e}\gamma_i\left(Q_{i\theta}^2+Q_{i\epsilon}^2\right) + \sum_{i\,\in\,t_1,\,t_2}\gamma_i\left(Q_{i\xi}^2+Q_{i\eta}^2+Q_{i\zeta}^2\right)\right]\mathbf{e}_\alpha\\ &+\frac{1}{2}\sum_{i\,\in\,e}\lambda_{ii}\left[\left(Q_{i\epsilon}^2-Q_{i\theta}^2\right)\mathbf{e}_\theta + Q_{i\theta}Q_{i\epsilon}\mathbf{e}_\epsilon\right] + \sum_{i\,\in\,t_2}\mu_{ii}^{t_2}\left(Q_{i\eta}Q_{i\zeta}\mathbf{t}_\xi + Q_{i\xi}Q_{i\zeta}\mathbf{t}_\eta + Q_{i\xi}Q_{i\eta}\mathbf{t}_\zeta\right)\end{aligned}$$

$$+\frac{1}{4}\sum_{i\in t_2}\mu_{ii}^{e}\left[\left(2Q_{i\zeta}^2-Q_{i\xi}^2-Q_{i\eta}^2\right)\mathbf{e}_\theta+\sqrt{3}\left(Q_{i\xi}^2-Q_{i\eta}^2\right)\mathbf{e}_\epsilon\right]$$
$$+\sum_{i,j\in e,t_2}b_{ij}\left[\left(-\frac{1}{2}Q_{i\theta}+\frac{\sqrt{3}}{2}Q_{i\epsilon}\right)Q_{j\xi}\mathbf{t}_\xi+\left(-\frac{1}{2}Q_{i\theta}-\frac{\sqrt{3}}{2}Q_{i\epsilon}\right)Q_{j\eta}\mathbf{t}_\eta+Q_{i\theta}Q_{j\zeta}\mathbf{t}_\zeta\right],$$

$$=\begin{pmatrix}\mathcal{W}_{11} & \mathcal{W}_{12} & \mathcal{W}_{13}\\ \mathcal{W}_{21} & \mathcal{W}_{22} & \mathcal{W}_{23}\\ \mathcal{W}_{31} & \mathcal{W}_{32} & \mathcal{W}_{33}\end{pmatrix}. \tag{6}$$

Where

$$\mathcal{W}_{11}=E_0+\sum_{i\in a_1}\kappa_iQ_i+\sum_{i\in e}\lambda_i\left(-\frac{1}{2}Q_{i\theta}+\frac{\sqrt{3}}{2}Q_{i\epsilon}\right)+\frac{1}{2}\Bigg[\sum_{i\in a_1,\,a_2}\gamma_iQ_i^2+\sum_{i\in e}\gamma_i(Q_{i\theta}^2+Q_{i\epsilon}^2)$$
$$+\sum_{i\in t_1,\,t_2}\gamma_i(Q_{i\xi}^2+Q_{i\eta}^2+Q_{i\zeta}^2)\Bigg]+\frac{1}{2}\sum_{i\in e}\lambda_{ii}\left(\frac{1}{2}Q_{i\theta}^2-\frac{1}{2}Q_{i\epsilon}^2+\sqrt{3}Q_{i\theta}Q_{i\epsilon}\right)$$
$$+\frac{1}{4}\sum_{i\in t_2}\mu_{ii}^{e}\left(2Q_{i\xi}^2-Q_{i\eta}^2-Q_{i\zeta}^2\right) \tag{7a}$$

$$\mathcal{W}_{22}=E_0+\sum_{i\in a_1}\kappa_iQ_i+\sum_{i\in e}\lambda_i\left(-\frac{1}{2}Q_{i\theta}-\frac{\sqrt{3}}{2}Q_{i\epsilon}\right)+\frac{1}{2}\Bigg[\sum_{i\in a_1,\,a_2}\gamma_iQ_i^2+\sum_{i\in e}\gamma_i(Q_{i\theta}^2+Q_{i\epsilon}^2)$$
$$+\sum_{i\in t_1,\,t_2}\gamma_i(Q_{i\xi}^2+Q_{i\eta}^2+Q_{i\zeta}^2)\Bigg]+\frac{1}{2}\sum_{i\in e}\lambda_{ii}\left(\frac{1}{2}Q_{i\theta}^2-\frac{1}{2}Q_{i\epsilon}^2-\sqrt{3}Q_{i\theta}Q_{i\epsilon}\right)$$
$$+\frac{1}{4}\sum_{i\in t_2}\mu_{ii}^{e}\left(2Q_{i\eta}^2-Q_{i\xi}^2-Q_{i\zeta}^2\right) \tag{7b}$$

$$\mathcal{W}_{33}=E_0+\sum_{i\in a_1}\kappa_iQ_i+\sum_{i\in e}\lambda_iQ_{i\theta}+\frac{1}{2}\Bigg[\sum_{i\in a_1,\,a_2}\gamma_iQ_i^2+\sum_{i\in e}\gamma_i(Q_{i\theta}^2+Q_{i\epsilon}^2)+\sum_{i\in t_1,\,t_2}\gamma_i(Q_{i\xi}^2+Q_{i\eta}^2+Q_{i\zeta}^2)\Bigg]$$
$$+\frac{1}{2}\sum_{i\in e}\lambda_{ii}\left(-Q_{i\theta}^2+Q_{i\epsilon}^2\right)+\frac{1}{4}\sum_{i\in t_2}\mu_{ii}^{e}\left(2Q_{i\zeta}^2-Q_{i\xi}^2-Q_{i\eta}^2\right) \tag{7c}$$

$$\mathcal{W}_{12}=\mathcal{W}_{21}=\sum_{i\in t_2}\left(\mu_iQ_{i\zeta}+\mu_{ii}^{t_2}Q_{i\xi}Q_{i\eta}\right)+\sum_{i,j\in e,t_2}b_{ij}Q_{i\theta}Q_{j\zeta} \tag{7d}$$

$$\mathcal{W}_{13}=\mathcal{W}_{31}=\sum_{i\in t_2}\left(\mu_iQ_{i\eta}+\mu_{ii}^{t_2}Q_{i\xi}Q_{i\zeta}\right)+\sum_{i,j\in e,t_2}b_{ij}\left(-\frac{1}{2}Q_{i\theta}-\frac{\sqrt{3}}{2}Q_{i\epsilon}\right)Q_{j\eta} \tag{7e}$$

$$\mathcal{W}_{23}=\mathcal{W}_{32}=\sum_{i\in t_2}\left(\mu_iQ_{i\xi}+\mu_{ii}^{t_2}Q_{i\eta}Q_{i\zeta}\right)+\sum_{i,j\in e,t_2}b_{ij}\left(-\frac{1}{2}Q_{i\theta}+\frac{\sqrt{3}}{2}Q_{i\epsilon}\right)Q_{j\xi}. \tag{7f}$$

$\mathbf{e}_\alpha$, $\mathbf{e}_\theta$ and $\mathbf{e}_\epsilon$, and $\mathbf{t}_\xi$, $\mathbf{t}_\eta$ and $\mathbf{t}_\zeta$ are the matrices containing appropriate coupling coefficients, which are defined in the space of $|\xi\rangle$, $|\eta\rangle$, $|\zeta\rangle$ of functions for the triply degenerate state at the reference geometry, along with a_1 and two components of e and three components of t_2 vibrational modes. The six matrices, as appear above, are as follows respectively: [11, 14, 15]

$$\begin{pmatrix} 1 & 0 & 0 \\ 0 & 1 & 0 \\ 0 & 0 & 1 \end{pmatrix}, \begin{pmatrix} -\frac{1}{2} & 0 & 0 \\ 0 & -\frac{1}{2} & 0 \\ 0 & 0 & 1 \end{pmatrix}, \begin{pmatrix} \frac{\sqrt{3}}{2} & 0 & 0 \\ 0 & -\frac{\sqrt{3}}{2} & 0 \\ 0 & 0 & 0 \end{pmatrix}, \begin{pmatrix} 0 & 0 & 0 \\ 0 & 0 & 1 \\ 0 & 1 & 0 \end{pmatrix}, \begin{pmatrix} 0 & 0 & 1 \\ 0 & 0 & 0 \\ 1 & 0 & 0 \end{pmatrix} \text{ and } \begin{pmatrix} 0 & 1 & 0 \\ 1 & 0 & 0 \\ 0 & 0 & 0 \end{pmatrix}.$$

The diagonal elements of the matrix in Eq. (6) present the diabatic potential energies of the three components of this electronic state while the off-diagonal elements are the corresponding couplings. The quantity E_0 is the vertical ionization energy for the ground $\widetilde{X}\,^2T_2$ electronic state of $C(CH_3)_4^+$. The linear coupling parameter of the totally symmetric a_1 vibrational mode is given by κ_i, and the linear JT coupling parameters for doubly degenerate e and triply degenerate t_2 vibrational modes are denoted by λ_i and μ_i, respectively. Note that γ_i are the diagonal second-order parameters along each vibrational mode. This actually amounts to the frequency change due to the electronic transition from ground $\widetilde{X}\,^1A_1$ electronic state of $C(CH_3)_4$ to the cationic $\widetilde{X}\,^2T_2$ state along those vibrations, respectively. Additionally, b_{ij} represents the bilinear JT coupling parameters which arise due to the coupling between the vibrational modes of e and t_2 symmetry. In turn, λ_{ii}, μ_{ii}^e and $\mu_{ii}^{t_2}$ refer to the quadratic JT coupling constants resulting from the non-totally symmetric tensor convolutions of the $e \times e$ and $t_2 \times t_2$ symmetrized direct products, respectively. Numerical values of all the above coupling parameters are determined by performing extensive *ab initio* electronic structure calculations (see section III).

B. Nuclear Dynamics

Using the above Hamiltonian, the vibronic spectrum of the $\widetilde{X}\,^2T_2$ state is examined. The intensity, $P(E)$, of the vibronic band is calculated by the Fermi's golden rule

$$P(E) = \sum_v \left| \langle \Psi_v^f | \hat{T} | \Psi_0^i \rangle \right|^2 \delta(E - E_v^f + E_0^i), \tag{8}$$

where $|\Psi_v^f\rangle$ represents the eigenstates of the vibronic Hamiltonian with energy E_v^f, and $|\Psi_0^i\rangle$ is the initial ground vibronic state of the neutral molecule with energy E_0^i. $\hat{T}$ is the operator that describes the interaction of the electrons with the external radiation, and E the electron binding energy (ionization energy). The initial vibronic state

$$|\Psi_0^i\rangle \;=\; |\Phi^0\rangle|\chi_0^0\rangle, \tag{9}$$

is represented as a product of the diabatic electronic ($|\Phi^0\rangle$) and vibrational ($|\chi_0^0\rangle$) components. The latter is the eigenfunction of the unperturbed reference Hamiltonian, $\mathcal{H}_0$. It should be noted that in the final vibronic state, $|\Psi_v^f\rangle$, the scattering wavefunction of the outgoing electron is missing. Similarly, the kinetic energy of the outgoing electron is missing in the Einstein condition of Eq. (8). In fact, the determination of the correct wavefunction of the final vibronic state is actually an intricate problem due to the fact that the scattering state belongs to the kinetic energy of the outgoing wave which behaves as a plane wave at an asymptotic distance but for shorter electron distances is modified due to interaction with the cation, a topic that is actually an active research area in nonadiabatic electron-scattering theory. [46–48] It should also be noted that the calculation of vibronic intensities close to the ionization threshold poses an additional intricacy by the the fact that it should verify the Wigner threshold law. [49] In the present case, we have used Franck-Condon factors to calculate the vibronic intensities for the $\widetilde{X}\,^2T_2$ state of $C(CH_3)_4^+$.

In a time-dependent picture, Eq. (8) can be related to a Fourier transform of the time autocorrelation function of the wave packet [50]

$$P(E) \sim 2Re \int_0^\infty e^{iEt/\hbar}\langle 0|\boldsymbol{\tau}^\dagger e^{-i\mathcal{H}t/\hbar}\boldsymbol{\tau}|0\rangle dt, \tag{10}$$

$$\sim 2Re \int_0^\infty e^{iEt/\hbar} C^m(t) dt. \tag{11}$$

The quantity, $C^m(t) = \langle\Psi^m(0)|\Psi^m(t)\rangle$, is the time autocorrelation function of the WP initially prepared on the m-th electronic state. $\boldsymbol{\tau}$ refers to the transition dipole matrix; $\boldsymbol{\tau}^\dagger = \left(\tau^{\widetilde{X_1}}\,,\,\tau^{\widetilde{X_2}}\,,\,\tau^{\widetilde{X_3}}\right)$, with τ^m=$\langle\Phi^m|\hat{T}|\Phi^0\rangle$; the dagger stands for transposed, and $\tilde{X}_i$ ($i = 1-3$) for the various degenerate potential sheets. As discussed above, we assume that the ejected electron does not correlate with the electrons of the ion and the involved matrix elements are set to unity. This is in consistent with the applicability of the Frank-

Condon approximation in a diabatic electronic basis. [50] The partial spectra are calculated by propagating WPs for three different initial conditions and convoluted them together to yield the final composite vibronic spectrum.

In a time-dependent method an appropriate WP is first prepared in the final electronic state of the cation and then propagated with the aid of the time-dependent Schrödinger equation, $i\hbar\partial_t|\Psi_v\rangle = \mathcal{H}|\Psi_v\rangle$. The autocorrelation function, $C^m(t)$, of the WP is recorded in time and Fourier transformed to finally calculate the vibronic spectrum via Eqs. (10) and (11). The WP propagation is carried out by employing the efficient MCTDH algorithm [39–43] which is the best suited one for full quantum mechanical simulation of multistate and multimode problems like the present one. The multi-set ansatz of the MCTDH algorithm allows a combination of vibrational degrees of freedom to effectively reduce the dimensionality of the problem. The WP associated with each electronic state is described using a different set of single particle functions (SPFs). By combining the nuclear degrees of freedom f, p numbers of particles are formed ($p < f$). The variables for the p sets of SPFs are defined in terms of the single- or multi-dimensional coordinates of a particle. The density matrices of the SPFs can be used to provide a useful measure of the quality of the calculation. The eigenfuctions of this matrix are termed *natural orbitals* and the eigenvalues provide populations for these functions. The lower the population, the less important the functions for the representation of the wavefunction. As the space spanned by the natural orbitals is equivalent to that of the originals SPFs, if the population of the highest natural orbital is such that the function is effectively not required for an accurate description of the evolving wavepacket, the MCTDH wavefunction is of good quality. As a rule of thumb averaged quantities such as expectation values and spectra are converged when the highest natural orbitals have a population below 1%. The operational principles of the MCTDH algorithm are discussed in detail in the literature [39–43] and we do not reiterate here.

III. EVALUATION OF COUPLING PARAMETERS

An accurate evaluation of the coupling parameters of the above devised Hamiltonian matrix is a key issue for the reproduction of the vibronic spectra and interpret the structural dynamics. To estimate such values, the adiabatic electronic PESs of the $\widetilde{X}\,^2T_2$ electronic state of $C(CH_3)_4^+$ are calculated along the dimensionless normal coordinates of the electronic

TABLE I: The equilibrium geometry of the electronic ground state of $C(CH_3)_4$ along with the available experimental data. Theoretical calculations are carried out at the MP2 level of theory employing the cc-pVDZ basis set. The distances (r) are given in Å and angles (a) are in degrees.

Description	This work	Experiment [53]
rCC	1.535	1.537
rCH	1.104	1.114
aHCC	110.9	112.2
aHCH	108.0	106.6

ground state ($\widetilde{X}\,^1A_1$) of $C(CH_3)_4$. The geometry optimization and calculation of harmonic vibrational frequencies of $C(CH_3)_4$ at the equilibrium geometry of its electronic ground state ($^1A_1$) are carried out at the second-order Møller-Plesset perturbation (MP2) level of theory employing the correlation-consistent polarized valence double-ζ (cc-pVDZ) basis set of Dunning [51] with the Gaussian-03 program. [52] The optimized geometry parameters of the electronic ground state of $C(CH_3)_4$ are given in Table I along with the available experimental results of Ref. [53]. It can be seen from Table I, that the theoretical results are in good accord with the experiment. [53]

The harmonic vibrational frequencies (ω_i) of $C(CH_3)_4$ are calculated by diagonalizing the *ab initio* force constant matrix. These vibrational frequencies are recorded in Table II along with their available experimental values. [54]. The symmetry and the dominant nature of the vibrations are also given in this Table. The mass-weighted normal coordinates of the vibrational modes are calculated from the eigenvectors of the force constant matrix. These are then multiplied with $\sqrt{\omega_i}$ (in a_0) to obtain the dimensionless normal coordinates (Q_i).

The adiabatic *ab initio* energies of the $\widetilde{X}\,^2T_2$ state of $C(CH_3)_4^+$ have been calculated along one and two dimensions in the normal mode coordinate space of the neutral $C(CH_3)_4$. We note that using a multi-reference wavefunction based method for calculating the above *ab initio* energies turned out to be computationally very expensive due to the high nuclear dimensionality of $C(CH_3)_4$. Therefore, we first calculated the vertical ionization energy (VIE) of $C(CH_3)_4$ at it's equilibrium nuclear configuration by the Outer Valence Green's Function (OVGF) method using the Gaussian 2003 package, [52] complete-active-space self-consistent-field (CASSCF) method using the Molpro 2010 package [55] and equation of motion ionization potential coupled cluster singles and doubles (EOM-IP-CCSD) method using CFOUR package [56] for calibrating the level of the theory for the present study. CASSCF calculations are carried out with various complete-active-space (CAS) wavefunc-

TABLE II: Description of the vibrational modes of the electronic ground state of $C(CH_3)_4$ computed at the MP2/cc-pVDZ level of theory. While the theoretical frequencies are harmonic in nature the experimental ones are fundamentals.

		Frequency (ω_i)/eV			
Symmetry	Mode	This work	Experiment [54]	Predominant Nature	Coordinate
a_1	ν_1	0.38024	0.36067	CH symmetric stretching	Q_1
	ν_2	0.17697	0.17122	CH_3 symmetric umbrella motion	Q_2
	ν_3	0.09339	0.09088	CC symmetric stretching	Q_3
a_2	ν_4	0.02596	0.02455	CH rocking (symmetric)	Q_4
e	ν_5	0.39173	0.36637	CH antisymmetric stretching	$Q_{5\theta}$, $Q_{5\epsilon}$
	ν_6	0.18379	0.17990	CH scissoring	$Q_{6\theta}$, $Q_{6\epsilon}$
	ν_7	0.13436	0.12386	CH rocking n	$Q_{7\theta}$, $Q_{7\epsilon}$
	ν_8	0.04103	0.04153	CC scissoring	$Q_{8\theta}$, $Q_{8\epsilon}$
t_1	ν_9	0.39230	0.36885	CH antisymmetric stretching	$Q_{9\xi}$, $Q_{9\eta}$, $Q_{9\zeta}$
	ν_{10}	0.18285	0.18114	CH scissoring	$Q_{10\xi}$, $Q_{10\eta}$, $Q_{10\zeta}$
	ν_{11}	0.11822	0.11555	CH twisting	$Q_{11\xi}$, $Q_{11\eta}$, $Q_{11\zeta}$
	ν_{12}	0.03633	0.02517	CH rocking	$Q_{12\xi}$, $Q_{12\eta}$, $Q_{12\zeta}$
t_2	ν_{13}	0.3983	0.36687	CH antisymmetric stretching	$Q_{13\xi}$, $Q_{13\eta}$, $Q_{13\zeta}$
	ν_{14}	0.37945	0.35658	CH stretching (symmetric within CH_3 group)	$Q_{14\xi}$, $Q_{14\eta}$, $Q_{14\zeta}$
	ν_{15}	0.18751	0.18288	CH deformation	$Q_{15\xi}$, $Q_{15\eta}$, $Q_{15\zeta}$
	ν_{16}	0.17257	0.17011	CH_3 antisymmetric umbrella motion	$Q_{16\xi}$, $Q_{16\eta}$, $Q_{16\zeta}$
	ν_{17}	0.16050	0.15572	H_3C-C stretching	$Q_{17\xi}$, $Q_{17\eta}$, $Q_{17\zeta}$
	ν_{18}	0.11891	0.11468	CC antisymmetric stretching	$Q_{18\xi}$, $Q_{18\eta}$, $Q_{18\zeta}$
	ν_{19}	0.05119	0.05183	CC umbrella bending	$Q_{19\xi}$, $Q_{19\eta}$, $Q_{19\zeta}$

TABLE III: Theoretical VIEs of the $\widetilde{X}\,^2T_2$ state of $C(CH_3)_4^+$ obtained in various methods, and CASs and CSFs used in CASSCF method along with the available experimental VIEs. Theoretical calculations are carried out employing the cc-pVDZ basis set. The VIEs are in eV.

Method	CAS (No. of correlated electrons, No. of active orbitals)	CSF	VIE
OVGF	-	-	11.245
CASSCF	(5,10)	830	12.522
CASSCF	(11,10)	6940	11.774
CASSCF	(11,13)	245488	11.827
CASSCF	(15,12)	47190	12.395
EOM-IP-CCSD	-	-	11.158
Experiment[57]	-	-	10.900
Experiment[58]	-	-	10.900±0.1
Experiment[36]	-	-	11.300

tions as references. In all references the C 1s core orbital was closed, but optimized in the CASSCF step. For the basis set, we have selected cc-pVDZ of Dunning. [51] The calculated VIEs, CAS and respective number of configuration state functions (CSFs) are given in Table III along with the experimental VIEs. It can be seen from Table III that the CASSCF is overestimating the VIE of $C(CH_3)_4$. While the EOM-IP-CCSD results into the closest value to the experimental observations it severely fails to satisfy the convergence criteria at distorted geometries from the equilibrium nuclear configuration. Therefore, in the present work we have employed OVGF level of theory as implemented in Gaussian 03 program. [52] It provides affordable computational cost and reasonably good accuracy.

The eigenvalues of the above 3×3 diabatic Hamiltonian matrix (excluding the kinetic energy of the nuclei) have then been fitted to the adiabatic *ab initio* ionization energies by a least-squares procedure to derive numerically the various coupling parameters as well as the adiabatic PESs. We note that the eigenvalues of a 3×3 matrix generically depend nonlinearly on the fitting parameters even if they appear linearly on each individual matrix element. To carry out the fit, the Levenberg-Marquardt algorithm [59, 60] has been utilized. It should be noted that there is no analytic solution for the present least-squares minimization problem.

In the first step, the vertical ionization energy of the $\widetilde{X}\,^2T_2$ electronic state is calculated along the ith vibrational mode (keeping others at their equilibrium value) at intervals of 0.5 for a range of $0 \leq |Q_i| \leq 5$. The PESs obtained were then used to determine the various coupling parameters of the one-dimensional potential of the model Hamiltonian constructed above. In the second step, the vertical ionization energies are calculated for

TABLE IV: Coupling parameters in Eqs. (3-7f) as obtained from OVGF/cc-pVDZ level of theory. All values are in eV.

Mode	$\kappa_i/\lambda_i/\mu_i$	γ_i	λ_{ii}/μ^e_{ii}	$\mu^{t_2}_{ii}$	b_{ij}
ν_2	-0.1412	-0.0177			
ν_3	0.0792	-0.0007			
ν_7	0.2229	-0.0301	-0.0281		
ν_{16}	0.2394	-0.0165	-0.0048	-0.0036	-0.0102
ν_{17}	0.2775	-0.0268	-0.0009	-0.0028	0.0260
ν_{19}	0.0878	0.0015	-0.0041	-0.0017	0.0025

the simultaneous displacements of two coordinates of e mode (both by an equal amount), two coordinates of t_2 modes, and one coordinate of e and one coordinate of t_2 modes. Then all the coupling parameters of the vibronic Hamiltonian of Eq. (6) were fitted to the *ab initio* energies obtained from the above displacements of nuclear geometry along the two dimensional subspace of the nuclear coordinates, keeping the parameters determined from the one dimensional cuts as the initial guess. The parameters that represent the best agreement between the model and the calculated *ab initio* energies are gathered in Table IV. Table IV immediately shows that not all 45 vibrational degrees of freedom play significant role in the nuclear dynamics. Therefore, the relevant modes having significant coupling strengths are retained only in this table for clarity. Such considerations result 13 nonseparable vibrational degrees of freedom are of crucial importance to describe the potential energy surfaces and the coupling surfaces of the diabatic electronic states.

IV. ADIABATIC POTENTIAL ENERGY SURFACES

In this section, we examine the topography of the adiabatic PESs of $\widetilde{X}\,^2T_2$ electronic state of $C(CH_3)_4^+$ to understand it's various static aspects. The model vibronic Hamiltonian used in the current study [Eqs. (3)-(7f)] is devised to reproduce the calculated adiabatic PESs under T_d symmetry within QVC scheme. As already noted, the various parameters of the potential matrix of the Hamiltonian are obtained by a least-squares fit of the eigenvalues to the *ab initio* data points. Resulting one-dimensional cuts of these multidimensional PESs along the dimensionless normal coordinate of each vibrational mode are shown in Figures 1, 2 and 3. In each plot, the points represent the computed *ab initio* adiabatic potential energies, and the curves superimposed on them are the fitted vibronic model of Section II.

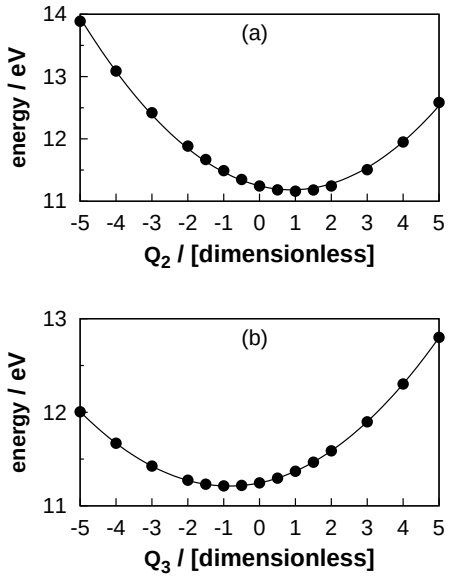

FIG. 1: Adiabatic potentials for the $\widetilde{X}\,^2T_2$ state of $C(CH_3)_4^+$ along the dimensionless totally symmetric vibrational modes, ν_2 and ν_3, respectively. Energy of the ground electronic state of $C(CH_3)_4$ ($\widetilde{X}\,^1A_1$) at equilibrium configuration ($\mathbf{Q=0}$) is set to zero. The present vibronic model is shown by the solid line and the computed *ab initio* data by the solid dots.

The calculated adiabatic energies of the $\widetilde{X}\,^2T_2$ electronic state along the totally symmetric vibrational modes of ν_2 and ν_3 are plotted in panels a and b of of Figure 1, respectively. It can be seen that the totally symmetric vibrations cannot lift the degeneracy of the $\widetilde{X}\,^2T_2$ electronic state and the locus of degeneracy of the three components of this state defines the seam of the threefold JT conical intersections. In a second-order vibronic coupling scheme, the minimum of these seams occurs at $Q_2^0 \sim 0.8865$ and $Q_3^0 \sim -0.8545$ in the space of ν_2 and ν_3 vibrational modes, respectively. The energetic minimum of these seams in a 2D hypersurface, developed from tuning active ν_2 and ν_3 vibrations, is predicted to be $\mathcal{V}_{min}^{(c)} \sim$ 11.1486 eV.

Similarly, the one-dimensional adiabatic potential energy cuts along both the components ($Q_{7\theta}$ and $Q_{7\epsilon}$) of the doubly degenerate ν_7 mode are shown in panels a and b of Figure 2. As seen from panels a and b of this Figure that the nuclear displacements along the $Q_{7\epsilon}$ component splits the triply degenerate $\widetilde{X}\,^2T_2$ electronic manifold into three nondegenerate electronic states, while that along the $Q_{7\theta}$ component yields a partial lifting, namely one doubly degenerate and one nondegenerate electronic states. Thus, it is necessary to fit them simultaneously and the best fitted results are depicted in panels b and a of Figure 2, in the

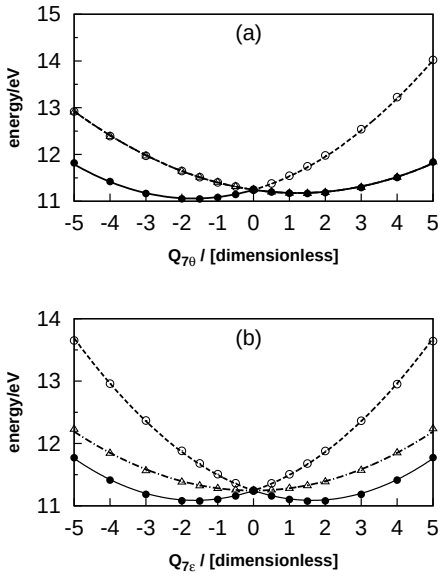

FIG. 2: Same as in Figure 1, along both components (θ and ϵ) of the doubly degenerate vibrational mode, ν_7.

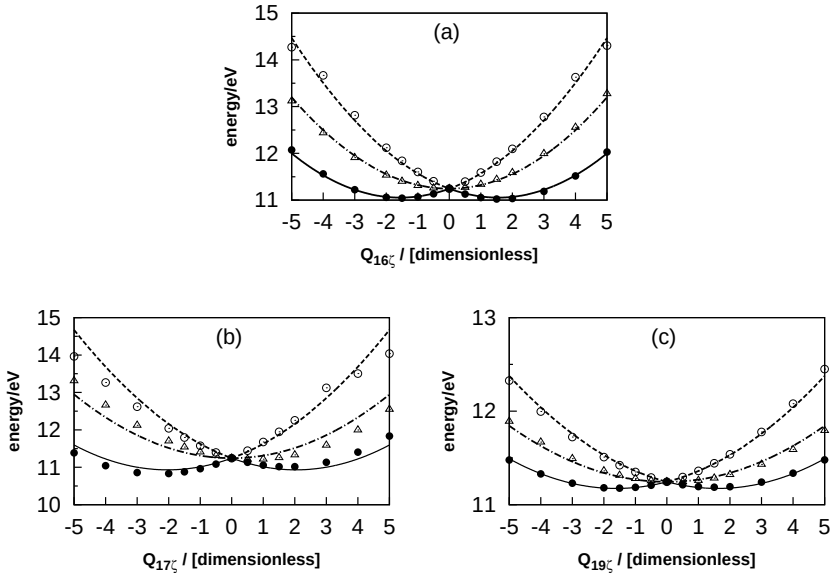

FIG. 3: Same as in Figure 1, along ζ component of the triply degenerate vibrational modes, ν_{16}, ν_{17} and ν_{19}, respectively

.

above order. The global root-mean-square errors estimated for the final fits are $\sim 1.5 \times 10^{-2}$ eV.

The electronic degeneracy of the $\widetilde{X}\,^2T_2$ state is also split when distortion is along the triply degenerate vibrational modes of t_2 symmetry, and this splitting leads to three nondegenerate

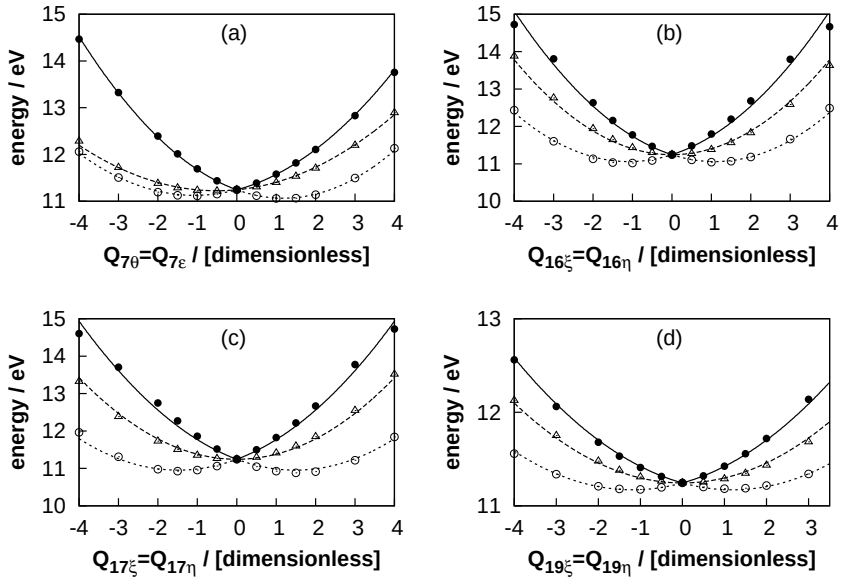

FIG. 4: Same as in Figure 1, along the simultaneous displacement of two coordinates of e(a) and t_2(b-d) vibrational modes.

state together. We note that any of the three vibrational components (Q_ξ, Q_η and Q_ζ) lift the triple electronic degeneracy in a way similar to that for a given t_2 mode. Thus we have shown the adiabatic potential energy cuts only along one component, *i.e.*, Q_ζ for brevity. The resulting potential energy cuts along that component of ν_{16}, ν_{17} and ν_{19} vibrational modes are illustrated in panels a, b and c of Figure 3, respectively. It can be seen from the above figures that the current model mimics well all *ab initio* data points.

So far we have calculated the adiabatic potential energies only along each of the single normal mode coordinates and fitted them by diagonalizing the above modeled diabatic vibronic coupling Hamiltonian with high accuracy. In the following, we examine the adiabatic potential energy cuts along the diagonal of two-dimensional (2D) subspace of the nuclear coordinates obtained by simultaneously displacing two JT active normal coordinates of e and t_2 symmetries. There are three possibilities: (i) the two coordinates correspond to the two components of the e mode; (ii) both belong to the t_2 mode; (iii) one belongs to the e mode and the other to the t_2 mode. The full matrix is fitted with the *ab initio* data points and the results are shown in Figures 4 and 5. As it can be seen from these two figures, our model Hamiltonian reproduces the diagonal of the various 2D hypersurfaces very well.

It is well established that the symmetry breaking due to JT distortion leads to new minima on the lowest adiabatic sheet of the $\widetilde{X}\,^2T_2$ electronic manifold. A symmetry breaking

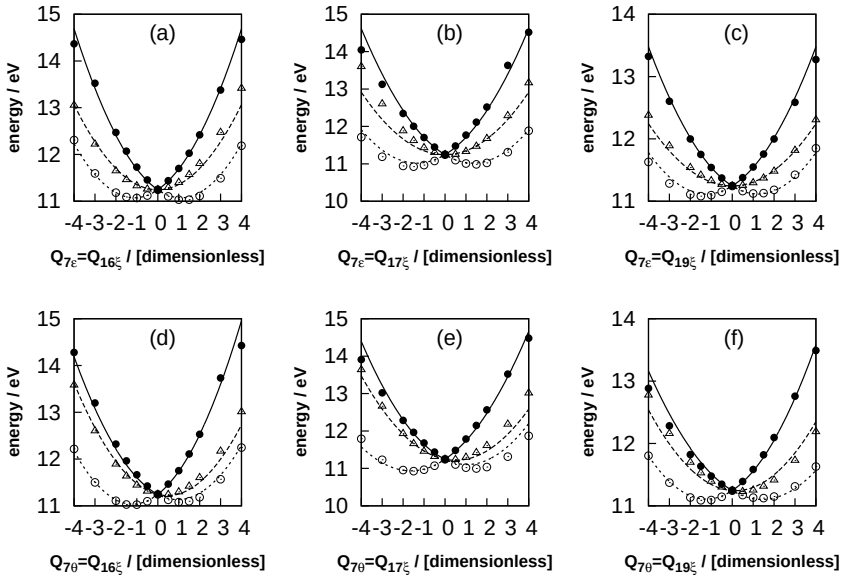

FIG. 5: Same as in Figure 1, long the simultaneous displacement of two coordinates of one component of e mode and one component of t_2 vibrational modes.

coordinate, say Q_α (where α stands for $\theta, \epsilon, \xi, \eta, or\ \zeta$) will reduce the original group G to one of its subgroups $S \subset G$. Which subgroup S is accessible by activating a specific JT active coordinate was discussed based on the group theoretical concept of kernels and epikernels. [61–63] Such an approach suggests that all the symmetry elements of G will be destroyed during the distortion except those that leave Q_α invariant. Therefore, in the subgroup S, Q_α will be totally symmetric, whereas in the parent group G, Q_α is not totally symmetric and is actually one of the basis vectors describing the multidimensional space of the JT active vibrations. The representations spanned by these vectors are denoted by Γ. For T_d group, Γ can be e and/or t_2. The kernel of a given representation Γ in G, denoted by $K(G, \Gamma)$, is the subgroup of G where all the basis functions of Γ become totally symmetric. Whereas an epikernel of Γ in G, denoted by $E(G, \Gamma)$, is also a subgroup of G but at least one basis function of Γ can be chosen to be invariant. [61] Thus, if Γ reduces to Γ' in the epikernel subgroup, Γ' should be reducible and contain totally symmetric basis function at least once. Therefore, the kernel is minimal epikernel.

In the present case, the kernel of e representation (containing two vibrational coordinates Q_θ and Q_ϵ) in T_d, $K(T_d, e)$=D_2, as the e vibrations destroy all T_d symmetry elements except for those belonging to D_2. Thus in D_2, both Q_θ and Q_ϵ (or any linear combination) have become totally symmetric. Therefore, D_2 is the lowest possible symmetry attainable by e

vibrations. Whereas in the intermediate D_{2d} group, only the Q_θ component of e vibration is invariant and thus the totally symmetric representation occurs only once in the decent in symmetry $T_d \rightarrow D_{2d}$. [64] Therefore D_{2d} is an epikernel $E(T_d, e)$ where the T_2 electronic degeneracy splits into two components of B_2 and E symmetry. Since E component is doubly degenerate, it remains JT unstable and undergoes further JT splitting when Q_ϵ (which is reduced to b_1 symmetry at D_{2d} geometry) coordinate is activated.[64] Energetics of such a splitting can be discussed by using a force constant approach,[65] where a molecule in a degenerate state can be said to be subject to a force corresponding to the slope of the energy curve in the high-symmetry origin. It is also well-known that the sum of the forces over all the electronic components in the origin is zero. Thus in the present case, the slope of the B_2 component at D_{2d} epikernel is twice as steep as the slope of E component. Therefore the B_2 state will be characterized by the ground state (deepest minimum) and E state will be the first excited state of the cation at D_{2d} epikernel.

The energy minimum of the Q_e space are thus situated in the epikernel (D_{2d}) rather than in kernel (D_2). This is a manifestation of epikernel principle [61–63]. While the JT theorem is based on the consideration of the forces in a highly symmetric degenerate state and predicts that the symmetry breaking coordinates moving the system into a lower symmetric configuration space, the epikernel principle on the contrary is based on the forces operating on the system in these lower symmetric points. For example the B_2 ground state of D_{2d} epikernel is in principle subject to forces parallel and perpendicular to Q_θ axis. However such a force $(B_2|\partial\mathcal{H}/\partial Q_\epsilon|B_2)$=0 since Q_ϵ is the basis for b_1 representation in D_{2d}. Whereas $(B_2|\partial\mathcal{H}/\partial Q_\theta|B_2) \neq 0$, being Q_θ totally symmetric in D_{2d}. Thus, D_{2d} structure will experience only totally symmetric distortion forces. On the other hand, the forces on D_2 structures in Q_ϵ plane is not restricted to any directions and can adopt arbitrary values.

Similarly the kernel of t_2 vibrations in T_d group is C_1, while the epikernels are C_{3v}, C_{2v} and C_s as the totally symmetric representation appears once in C_{3v} and C_{2v}, twice in C_s and three times in C_1. [64] The above discussions reveal that the extremal points of the molecular ground state will be situated in high-symmetry epikernels C_{3v}, C_{2v} as there can be no forces driving it into surrounding zone of lower symmetry. [16] Therefore, as far as minima and saddle points are concerned, not only epikernels are preferred over kernels, but the maximal epikernels are preferred over lower ranking epikernels. [16] Similarly, C_{2v} is the maximal epikernel in the five dimensional space (Q_e, Q_{t_2}) of combined $(e + t_2)$ vibrations.

TABLE V: JT stabilization energies for $T_2 \otimes e$, $T_2 \otimes t_2$ and $T_2 \otimes (t_2 + e)$ distortion on the electronic ground state of CH_4^+ and $C(CH_3)_4^+$. All the values are in eV.

JT problem	resulting maximal epikernel	CH_4^+	$C(CH_3)_4^+$
$T_2 \otimes e$	D_{2d}	1.1130	0.1849
$T_2 \otimes t_2$	C_{3v}	0.8020	0.6417
$T_2 \otimes (e + t_2)$	C_{2v}	1.1580	0.6199

Therefore, the minimum of the ground electronic state in this space are most likely to be found in C_{2v} structures.

Thus the epikernel principle implies that the three maximal epikernels of T_d geometry of the $\widetilde{X}\,^2T_2$ electronic state, D_{2d}, C_{3v} and C_{2v}, can all give rise to complete minima. Which one of the complete minima would be the absolute minimum, depends on the amount of JT stabilization energy they would gain due to the formation of the above epikernels. We have estimated the JT stabilization energies within the first-order vibronic coupling scheme. In view of epikernel principle, first we have calculated the JT stabilization energies for $T_2 \otimes e$- and $T_2 \otimes t_2$-JT problem. While the former distortion leading to D_{2d} epikernel by activating only Q_θ, the later yields C_{3v} maximal epikernel by distorting the cation simultaneously and equally via three components of t_2 mode (Q_ξ, Q_η and Q_ζ). Finally, we have estimated the JT stabilization energy for $T_2 \otimes (t_2 + e)$-JT problem which leads to C_{2v} maximal epikernel by activating Q_θ and one component of t_2 mode, say Q_ξ. All the results are shown in Table V. Similar results for CH_4^+ are also included in Table V for comparison.

It can be seen form Table V that for $C(CH_3)_4^+$, the JT stabilization energy due to the doubly degenerate ν_7 vibration is predicted to be $\frac{\lambda_7^2}{2\omega_7}$ $\sim$0.1849 eV and the same due to the triply degenerate ν_{16}, ν_{17} and ν_{19} vibrational modes amounts to $\sum_i \frac{2\mu_i^2}{3\omega_i}$ $\sim$0.6417 eV corresponding to newly formed minima on the lowest adiabatic sheet of $\widetilde{X}\,^2T_2$ electronic manifold of $C(CH_3)_4^+$. Whereas the JT stabilization energy of the new minimum occurs on the 11D hypersurface developed from the combination of above e and t_2 vibrations is estimated to be $\sum_i \frac{\lambda_7^2\omega_i + 4\mu_i^2\omega_7}{8\omega_7\omega_i}$ $\sim$0.6199 eV only. Therefore the C_{3v} epikernel arises from $T_2 \otimes t_2$-JT distortion is the absolute minimum occurs on the lowest adiabatic sheet of the $\widetilde{X}\,^2T_2$ electronic state of $C(CH_3)_4^+$. Similar results of CH_4^+, shown in Table V, are illustrating that the D_{2d} epikernel along e mode is preferred over C_{3v}. However, the JT distortion due to the combination of e and t_2 modes further stabilizes the D_{2d} to C_{2v} epikernel.

Additionally, the above discussion reveals that the T_2 electronic degeneracy splits into

two components of B_2 and E symmetry at D_{2d} epikernel where B_2 is characterized as the ground state and E as the excited electronic state. Accordingly, the JT active vibrations e and t_2 are reduced to $e = a_1 + b_1$ and $t_2 = b_2 + e$. Since the excited state is doubly degenerate it further splits into two nondegenerate states of B_1 and B_2 symmetry via $E \otimes b_2$ JT coupling, yielding the molecule into a C_{2v} geometry. At C_{2v} geometry, the B_2 ground state of D_{2d} epikernel is transformed to A_1 symmetry. Therefore, the earlier reported B_1 symmetry of the ground state of the C_{2v} structure of CH_4^+ is clearly connected to the excited E state of the D_{2d}. Thus a $T_2 \otimes (e + t_2)$ JT coupling distorts the CH_4^+ to a C_{2v} geometry in the ground state. A Similar mechanism for the observed C_{2v} geometry of the CH_4^+ is also suggested by our calculated JT stabilization energies shown in Table V. Whereas in case of $C(CH_3)_4^+$, the T_2 term of T_d geometry is splitted to A_1 and E terms at C_{3v} epikernel along simultaneous and equal displacements of Q_ξ, Q_η and Q_ζ coordinates of t_2 vibrations where the A_1 terms is characterized as the ground state and the E term as the excited state. While the ground A_1 state is JT inactive the excited E state undergoes $E \otimes e$ JT splitting at this C_{3v} geometry and the molecule is distorted into a C_s geometry. However a comparison of our calculated JT stabilization energies (cf., Table V) suggests that the minimum energy of the lower JT distorted sheet of the excited E state is higher than the minimum energy of the A_1 ground state of the C_{3v} geometry. We note that the differences of JT stabilization energies of $T_2 \otimes (e + t_2)$ vs. $T_2 \otimes e$ for CH_4^+ is $\sim$0.045 eV, and $T_2 \otimes (e + t_2)$ vs. $T_2 \otimes t_2$ for $C(CH_3)_4^+$ is $\sim$0.0218 eV, respectively, are rather small (3-4%). Therefore, these values are below the estimated accuracy of the *ab initio* method employed here. Certainly, more accurate *ab initio* calculations are desirable but unfortunately they are very expensive due to the size of a molecule like $C(CH_3)_4$. Furthermore, these values are the relative energies with respect to the energy of the undistorted T_d structure of the respective cations. Therefore, the above results can suggest that while JT active e and t_2 vibrations distort CH_4^+ into a C_{2v} minimum energy structure, the C_{3v} minimum energy configuration of $C(CH_4)^+$ occurs via t_2 vibrations. Thus our proposed mechanism for the appearance of different geometries of the title cations on their ground state mimics the experimental observations very well. [19–23, 32].

V. PHOTOELECTRON SPECTRUM

In this section we present the photoelectron spectrum underlying the $\widetilde{X}\,^2T_2$ electronic manifold of $C(CH_3)_4^+$. Such a spectrum obtained by employing the above modeled diabatic Hamiltonian [(cf., Eqs. (3)-(7f)] is shown in Figure 6 along with the spectrum recorded from He I photoelectron spectroscopy experiment by Murrell and Schmidt. [36] As discussed in

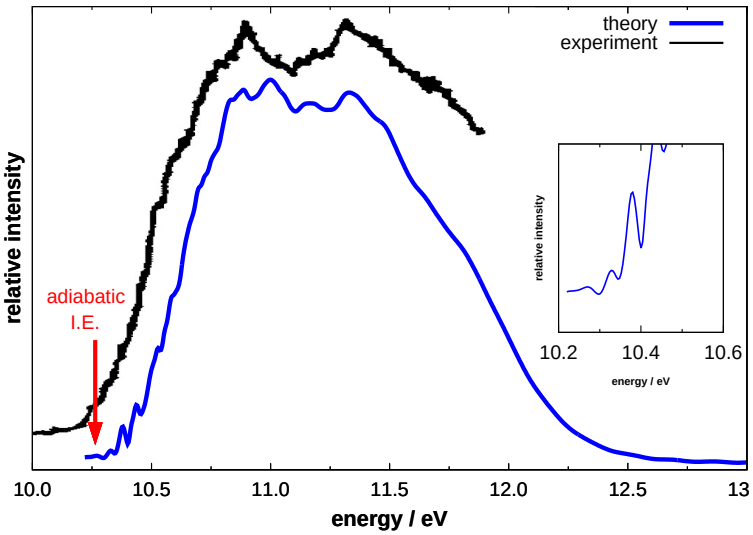

FIG. 6: Vibronic band of the $\widetilde{X}\,^2T_2$ electronic state of $C(CH_3)_4^+$. The intensity (in arbitrary units) is plotted along the energy (relative to minimum of the $\widetilde{X}\,^1A_1$ state of $C(CH_3)_4$) of the final vibronic states. The inset shows a magnified view for $10.2 \leq \text{energy/eV} \leq 10.6$.

the previous subsections, two a_1 (ν_2 and ν_3), one e (ν_7) and three t_2 (ν_{16}, ν_{17} and ν_{19}) modes may have an important role on the highly overlapping and structureless first photoelectron band of $C(CH_3)_4$. We follow therefore the nuclear dynamics simultaneously on the three diabatically coupled sheets of the $\widetilde{X}\,^2T_2$ electronic manifold including all the relevant vibrational degrees of freedom. This leads to a Hamiltonian matrix of huge dimension, and the associated Schrödinger equation cannot be solved by direct diagonalization. Thus, we solve the Schrödinger equation by propagating WPs within a time-dependent framework using the MCTDH algorithm, [39–43] and obtain the eigenvalue spectrum. The normal mode combinations, sizes of primitive and single particle basis to prepare the WP for $C(CH_3)_4^+$ are shown in Table VI.

Three calculations are carried out by initially preparing the WP separately on each component of the $\widetilde{X}\,^2T_2$ electronic manifold. The WP is propagated for 200 fs in each calculation. The time autocorrelation functions from the above three calculations are combined, damped

TABLE VI: Normal mode combinations, sizes of both primitive and single-particle basis used for propagating WP on the diabatically coupled electronic manifold employing the complete vibronic Hamiltonian of Eqs. (3-7f). First column denotes the vibrational degrees of freedom (DOF) which are combined to particles. Second column gives the number of primitive basis functions for each DOF. Third column gives the number of single particle functions (SPFs) for each JT splitted electronic state. Population of the highest natural orbitals are also included in column four.

Normal modes	primitive basis	SPF basis	population of the highest natural orbital
($\nu_{17\xi}$, $\nu_{7\epsilon}$, $\nu_{16\zeta}$, ν_2)	(18, 18, 12, 28)	[12, 11, 13]	[0.010, 0.010, 0.008]
($\nu_{17\eta}$, $\nu_{7\theta}$, $\nu_{16\eta}$, ν_3)	(18, 18, 12, 24)	[12, 13, 11]	[0.010, 0.008, 0.012]
($\nu_{17\zeta}$, $\nu_{16\xi}$, $\nu_{19\eta}$)	(18, 12, 12)	[10, 10, 11]	[0.017, 0.014, 0.008]
($\nu_{19\xi}$, $\nu_{19\zeta}$)	(12, 12)	[10, 11, 10]	[0.018, 0.008, 0.019]

with an exponential function to account for experimental line broadening effects, e^{-t/τ_r} (with τ_r=33 fs), and finally Fourier transformed to calculate the vibronic band of this $\widetilde{X}\,^2T_2$ electronic state. The value of τ_r used in the damping function corresponds to a convolution of the vibronic line spectrum with a Lorentzian function of 40 meV FWHM. The simulated spectrum envelope displayed in Figure 6, is in good agreement with the experimental spectrum. [36] Both the characteristic line structure, spectral intensity and the width of the vibronic band are well reproduced by the present QVC scheme. Our estimated adiabatic ionization energy of ∼10.27 eV is very close to the experimental observation of Evans and coworkers, who found this to be ∼10.25 eV. [35] Additionally, the JT splitting in this photoelectron band amounts to ∼0.45 eV is also in good accord with experimentally recorded value of ∼0.50 eV. [35]

In the following, we discuss the dominant vibrational progressions underlying this photoelectron band. Precise quantitative information on the vibronic energy levels could not be extracted from the poorly resolved experimental spectra; [35, 36] however we predicted them from the current model Hamiltonian. For such a prediction, we first construct various reduced-dimensionality models in terms of a_1, e, and t_2 vibrational modes, and examine the vibrational energy levels separately. These results help to understand the role of various vibrational modes in the complex vibronic structure of $C(CH_3)_4^+$ ($\widetilde{X}\,^2T_2$). The vibronic energy eigenvalues are obtained by diagonalizing the Hamiltonian matrix using the Lanczos algorithm. [44] Resulting three partial spectra due to a_1, e and t_2 vibrational modes are shown in panels a, b and c of Figure 7, respectively.

The fundamental and overtones up to third-order are excited for both the totally symmetric ν_2 and ν_3 modes. A corresponding peak spacings of ∼0.1679 eV and ∼0.0930 eV

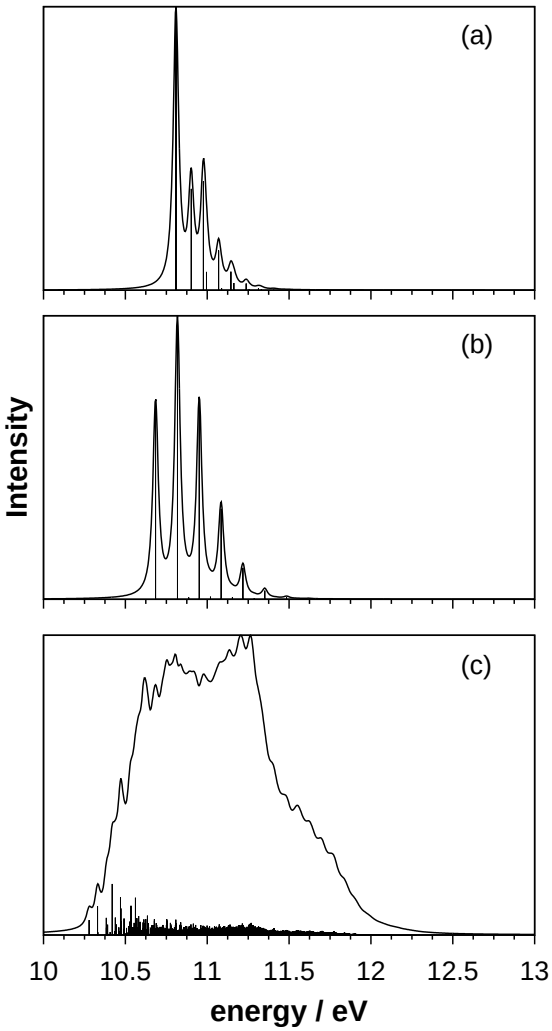

FIG. 7: Vibrational energy levels of the $\widetilde{X}\,^2T_2$ electronic manifold of $C(CH_3)_4^+$: (a) partial spectrum computed with the totally symmetric a_1 vibrational modes ν_2 and ν_3, (b) partial spectrum computed with the JT active doubly degenerate e vibrational mode ν_7, and (c) partial spectrum computed with three JT active triply degenerate t_2 vibrational modes ν_{16}, ν_{17} and ν_{19}. The intensity (in arbitrary units) is plotted as a function of the energy of the final vibronic state. The zero of energy corresponds to the equilibrium of the electronic ground state $C(CH_3)_4$. The theoretical stick spectrum in each panel in convoluted with a Lorentzian function of 40 FWHM to generate the spectral envelope.

can be estimated from the calculated partial spectrum (panel a) for the ν_2 and ν_3 vibrations, respectively. Additionally $\nu_2+\nu_3$, $2\nu_2+\nu_3$ and $\nu_2+2\nu_3$ combinations are also excited. A similar spectrum due to the doubly degenerate ν_7 vibrational mode (panel b) reveals the excitations of fundamental and overtones up to fourth-order. A line spacing of $\sim 0.1333\,\text{eV}$ is predicted. The partial spectrum due to triply degenerate ν_{16}, ν_{17} and ν_{19} vibrations (panel

c) reveals an extended progression due to strong JT activity and multimode effects. The intense lines are $\sim 0.1604\,\mathrm{eV}$, $\sim 0.1410\,\mathrm{eV}$ and $\sim 0.0520\,\mathrm{eV}$ spaced relative to the band origin corresponding to the frequency of the ν_{16}, ν_{17} and ν_{19} vibrational modes, respectively. However, the JT activity of the triply degenerate H_3C-C stretching ν_{17} mode is stronger than the triply degenerate ν_{16} and ν_{19} modes and forms the dominant progression underlying the partial spectrum obtained due to t_2 vibrations. Therefore, the strong excitations of this vibration yield the C_{3v} minimum energy structures of $C(CH_3)_4^+$ in it's ground electronic state. A careful look at the three partial spectra shown in various panels of Figure 7 indicates that the lowest energy transition appears from the t_2 vibrations. Furthermore, we have estimated that the first two peak in the partial spectrum of t_2 vibration is due to the excitations of ν_{19} vibration. Thus the oscillatory structures observed in low energy region of the $\widetilde{X}\,^2T_2$ photoelectron band of $C(CH_3)_4$ (cf. Figure 6) are due to ν_{19} excitations.

VI. SUMMARY AND OUTLOOK

A detailed theoretical analysis of the multimode JT interactions for the triply degenerate lowest electronic state ($\widetilde{X}\,^2T_2$) of $C(CH_3)_4^+$ has been performed to understand the origin of it's different structural symmetry compared to CH_4^+ as well as to elucidate the highly complex vibronic structure of the first photoelectron band of $C(CH_3)_4$. The necessary Hamiltonian has been developed from extensive *ab initio* electronic structure calculations and the underlying PESs have been established through various one- and two- dimensional cuts along the normal mode coordinate space of $C(CH_3)_4$. In order to get them in analytic form, the various coupling parameters of the vibronic Hamiltonian have been determined by fitting the eigenvalues of the matrix Hamiltonian to the *ab initio* calculated adiabatic potential energy surfaces along all the relevant vibrational modes and their two dimensional combinations thereof. First principles calculations have then been carried out with time-dependent quantal methods to simulate the nonadiabatic nuclear motion on this coupled electronic manifold. The theoretical results are in good agreement with the experimental observations. [35, 36]. A careful examination of various theoretical results reveal that: (a) totally symmetric ν_2 and ν_3 vibrations are strongly excited in the first photoelecton band of $C(CH_3)_4$; (b) the JT activity of the triply degenerate H_3C-C stretching vibration, ν_{17}, is stronger than the triply degenerate ν_{16} and ν_{19} vibrations and forms dominant progression in the partial spectrum

obtained due to t_2 mode; (c) the highly diffuse and overlapping first photoelectron band arises due to strong JT activity of the doubly degenerate ν_7 and triply degenerate ν_{16}, ν_{17} and ν_{19} vibrational modes within the $\widetilde{X}\,^2T_2$ electronic manifold of $C(CH_3)_4^+$; (d) the oscillatory structures observed in low energy region of the $\widetilde{X}\,^2T_2$ photoelectron band of $C(CH_3)_4$ are due to ν_{19} excitations. We have also calculated the JT stabilization energies of the $T_2 \otimes e$, $T_2 \otimes t_2$ and $T_2 \otimes (e + t_2)$ distortions in the $\widetilde{X}\,^2T_2$ electronic manifold of $C(CH_3)_4^+$ and found that such a stabilization energy is highest for $T_2 \otimes t_2$-JT distortion. Similar calculations on CH_4^+ estimates the highest JT stabilization energy due to $T_2 \otimes (e + t_2)$-JT distortion. [28, 29] From this observations and applying the epikernel principle, we proposes that while a combination of JT active e and t_2 vibrations leading to the C_{2v} minimum energy structure in case of ground state CH_4^+, the $T_2 \otimes t_2$-JT distortion yields the ground state $C(CH_3)_4^+$ at C_{3v} minimum energy configuration.

acknowledgement

This work is supported by an INSPIRE Faculty award of the Department of Science and Technology, New Delhi, India (INSPIRE Code [IFA-13 CH-92], Project No. DST/INSPIRE Faculty Award/2013/CH-92).

[1] H. A. Jahn and E. Teller, *Proc. R. Soc. London Ser. A*, 1937, **161**, 220-235.

[2] U. Opik and M. H. L. Pryce, *Proc. R. Soc. London Ser. A*, 1957, **238**, 425-447.

[3] H. C. Longuet-Higgins, U. Opik, M. H. L. Pryce and R. A. Sack, *Proc. R. Soc. London Ser. A*, 1958, **244**, 1-16.

[4] H. C. Longuet-Higgins, *Adv. Spectrosc.*, 1961, **2**, 429-472.

[5] R. Englman, *The Jahn-Teller Effect in Molecules and Crystals*; Wiley: New York, 1972;.

[6] H. Köppel, W. Domcke and L. S. Cederbaum, *Adv. Chem. Phys.*, 1984, **57**, 59-246.

[7] I. B. Bersuker, *Chem. Rev.* 2001, **101**, 1067-1114.

[8] I. B. Bersuker, *The Jahn-Teller Effect*; Cambridge University Press, Cambridge (U.K), 2006; 1-632.

[9] H. Köppel, L. S. Cederbaum and S. Mahapatra, *Theory of the Jahn-Teller Effect* in: Handbook

of high resolution spectroscopy, edited by M. Quack and F. Merkt, Wiley, Chichester, 2011.

[10] J. H. Van Vleck, *J. Chem. Phys.*, 1939, **7**, 72-84.

[11] W. Moffitt and W. Thorson, *Phys. Rev.*, 1957, **108**, 1251-1255.

[12] M. D. Sturge, in *Solid State Physics: Advances in Research and Applications*, edited by F. Seitz, D. Turnbull, and H. Ehrenreich Academic, New York, 1967, **20**, 91.

[13] M. C. M O'Brien, *Phys. Rev.*, 1969 **187**, 407-418

[14] I. B Bersuker and V. Z. Polinger, *Phys. Lett. A*, 1973, **44**, 495-496.

[15] I. B Bersuker and V. Z. Polinger, *Sov. Phys. JETP.*, 1974, **39**, 1023-1029.

[16] A. Ceulemans, D. Beyens and L. G. Vanquickenborne, *J. Am. Chem. Soc.*, 1984, **106**, 5824-5837.

[17] M. N. Paddon-Row, D. J. Fox, J. A. Pople, K. N. Houk and D. W. Pratt, *J. Am. Chem. Soc.* 1985 **107**, 7696-7700.

[18] R. F. Frey and E. R Davidson, *J. Chem. Phys.*, 1988, **88**, 1775-1785.

[19] L. B. Knight, Jr., J. Steadman, D. Feller and E. R. Davidson, *J. Am. Chem. Soc.*, 1984 **106**, 3700-3701.

[20] L. B. Knight, Jr., G. M. King, J. T. Petty, M. Matsushita, T. Momose and T. Shida, *J. Chem. Phys.*, 1995, **103**, 3377-3385.

[21] Z. Vager, E. P. Kanter, Both, P. J. Cooney, A. Faibis, W. Koenig, B. J. Zabransk and D. Zajfman, *Phys. Rev. Lett.*, 1986 **57**, 2793-2795.

[22] R. Signorell and F. Merkt, *Faraday Discuss.*, 2000 **115**, 205-228.

[23] H. J. Wörner and F. Merkt, *Angew. Chem. Int. Ed.*, 2009 **48**, 6404-6424.

[24] D. Opalka and W. Domcke, *J. Chem. Phys.*, 2010, **132**, 154108.

[25] D. Opalka and W. Domcke, *Chem. Phys. Lett.*, 2010, **494**, 134.

[26] D. Opalka and W. Domcke, *J. Chem. Phys.*, 2013, **138**, 224103.

[27] T. Mondal and A. J. C. Varandas, *J. Chem. Phys.*, 2011, **135**, 174304.

[28] T. Mondal and A. J. C. Varandas, *J. Chem. Phys.*, 2012, **137**, 214320.

[29] T. Mondal and A. J. C. Varandas, *J. Chem. Theory Comput.*, 2014, **10**, 3606-3616.

[30] T. Mondal and A. J. C. Varandas, *J. Chem. Phys.*, 2015, **143**, 014304.

[31] M. Iwasaki, K. Toriyama and K. Nunome, *J. Am. Chem. Soc.*, 1981, **103**, 3591-3592.

[32] K. Toriyama, K. Nunome and M. Iwasaki, *J. Chem. Phys.*, 1982, **77**, 5891-5912.

[33] K. Toriyama, M. Okazaki and K. Nunome, *J. Chem. Phys.*, 1991, **95**, 3955-3963.

[34] K. Toriyama and M. Okazaki, *Appl. Magn. Reson.*, 1994, **7**, 495-506.

[35] S. Evans, J. C. Green, P. J. Joachim, A. F. Orchard, D. W. Turner and J. P Maier, *J. Chem. Soc., Faraday Trans. 2*, 1972, **68**, 905-911.

[36] J. N Murrell and W. Schmidt, *J. Chem. Soc., Faraday Trans. 2*, 1972, **68**, 1709-1718.

[37] H. Shiromaru and S. Karsumata, *Bull. Chem. Soc. Jpn.*, 1984, **57**, 3543-3551.

[38] C. Cauletti, S. Sorensen and M. de Simone, *J. Electron. Spectrosc. Relat. Phenom.*, 1996, **79**, 457-461.

[39] G. A Worth, M. H. Beck, A. Jäckle and H. -D. Meyer The MCTDH Package, Version 8.2, 2000, University of Heidelberg, Germany. H.-D. Meyer, Version 8.3, 2002. See http://www.pci.uni-heidelberg.de/tc/usr/mctdh/

[40] H. D. Meyer, U. Manthe and L. S. Cederbaum, *Chem. Phys. Lett.*, 1990, **165**, 73-78.

[41] U. Manthe, H. D. Meyer and L. S. Cederbaum, *J. Chem. Phys.*, 1992, **97**, 3199-3213.

[42] M. H. Beck, A. Jäckle, G. A. Worth and H. D. Meyer, *Phys. Rep.*, 2000, **324**, 1-105.

[43] *Multidimensional Quantum Dynamics : MCTDH Theory and Applications*, edited by Meyer, H. -D., Gatti, F., Worth, G. A., WILEY-VCH, Weinheim, Germany, 2009; 1-446 .

[44] J. Cullum and R. Willoughby, *Lanczos Algorithms for Large Symmetric Eigenvalue Problems*; Birkhäuser, Boston, 1985, Vols. I and II.

[45] H. Köppel and W. Domcke, In *Encyclopedia of Computational Chemistry, P. V. R. Schleyer, Ed.*; Wiley: New York, 1998, p 3166.

[46] S. Han and D. R. Yarkony, *J. Chem. Phys.*, 2010, **133**, 194107.

[47] S. Han and D. R. Yarkony, *J. Chem. Phys.*, 2011, **134**, 134110.

[48] S. Han and D. R. Yarkony, *J. Chem. Phys.*, 2011, **134**, 174104.

[49] E. P. Wigner, *Phys. Rev.*, 1948, **73**, 1002-1009.

[50] W. Domcke, H. Köppel and L. S. Cederbaun, *Mol. Phys.*, 1981, **43**, 851-875.

[51] T. H. Dunning, Jr. *J. Chem. Phys.*, 1989, **90**, 1007-1023.

[52] Frisch, M. J.; Trucks, G. W.; Schlegel, H. B.; Scuseria, G. E.; Robb, M. A.; Cheeseman, J. R.; Montgomery, Jr., J. A.; Vreven, T.; Kudin, K. N.; Burant, J. C.; Millam, J. M.; Iyengar, S. S.; Tomasi, J.; Barone, V.; Mennucci, B.; Cossi, M.; Scalmani, G.; Rega, N.; Petersson, G. A.; Nakatsuji, H.; Hada, M.; Ehara, M.; Toyota, K.; Fukuda, R.; Hasegawa, J.; Ishida, M.; Nakajima, T.; Honda, Y.; Kitao, O.; Nakai, H.; Klene, M.; Li, X.; Knox, J. E.; Hratchian, H. P.; Cross, J. B.; Bakken, V.; Adamo, C.; Jaramillo, J.; Gomperts, R.; Stratmann, R. E.;

Yazyev, O.; Austin, A. J.; Cammi, R.; Pomelli, C.; Ochterski, J. W.; Ayala, P. Y.; Morokuma, K.; Voth, G. A.; Salvador, P.; Dannenberg, J. J.; Zakrzewski, V. G.; Dapprich, S.; Daniels, A. D.; Strain, M. C.; Farkas, O.; Malick, D. K.; Rabuck, A. D.; Raghavachari, K.; Foresman, J. B.; Ortiz, J. V.; Cui, Q.; Baboul, A. G.; Clifford, S.; Cioslowski, J.; Stefanov, B. B.; Liu, G.; Liashenko, A.; Piskorz, P.; Komaromi, I.; Martin, R. L.; Fox, D. J.; Keith, T.; Al-Laham, M. A.; Peng, C. Y.; Nanayakkara, A.; Challacombe, M.; Gill, P. M. W.; Johnson, B.; Chen, W.; Wong, M. W.; Gonzalez, C.; and Pople, J. A. *Gaussian 03*, Revision C.02; Gaussian, Inc.: Wallingford, CT, 2004.

[53] Kuchitsu (ed.), Landolt-Bornstein: Group II: Atomic and Molecular Physics Volume 15: Structure Data of Free Polyatomic Molecules. Springer-Verlag, Berlin, 1987.

[54] L. M. Sverdlov, M. A. Kovner and E. P. Krainov, Vibrational Spectra of Polyatomic Molecules. Wiley, New York 1974

[55] Werner, H. J.; Knowles, P. J.; Knizia, G.; Manby, F. R.; Schütz, M.; Celani, P.; Korona, T.; Lindh, R.; Mitrushenkov, A.; Rauhut, G.; Shamasundar, K. R.; Adler, T. B.; Amos, R. D, Bernhardsson, A.; Berning, A.; Cooper, D. L.; Deegan, M. J. O.; Dobbyn, A. J.; Eckert, F.; Goll, E.; Hampel, C.; Hesselmann, A.; Hetzer, G.; Hrenar, T.; Jansen, G.; Köppl, C.; Liu, Y.; Lloyd, A. W.; Mata, R. A.; May, A. J. McNicholas, S. J.; Meyer, W.; Mura, M. E.; Nicklass, A.; O'Neill, D. P.; Palmieri, P.; Pflüger, K.; Pitzer, R.; Reiher, M.; Shiozaki, T.; Stoll, H.; Stone, A. J.; Tarroni, R.; Thorsteinsson, T.; Wang, M.; Wolf, A. *Molpro*, version 2010.1; a package of ab initio programs, 2010. see http://www.molpro.net.

[56] CFOUR, a quantum chemical program package written by J.F. Stanton, J. Gauss, M.E. Harding, P.G. Szalay with contributions from A.A. Auer, R.J. Bartlett, U. Benedikt, C. Berger, D.E. Bernholdt, Y.J. Bomble, L. Cheng, O. Christiansen, M. Heckert, O. Heun, C. Huber, T.-C. Jagau, D. Jonsson, J. Juslius, K. Klein, W.J. Lauderdale, F. Lipparini, D.A. Matthews, T. Metzroth, L.A. Mck, D.P. O'Neill, D.R. Price, E. Prochnow, C. Puzzarini, K. Ruud, F. Schiffmann, W. Schwalbach, C. Simmons, S. Stopkowicz, A. Tajti, J. Vzquez, F. Wang, J.D. Watts and the integral packages MOLECULE (J. Almlf and P.R. Taylor), PROPS (P.R. Taylor), ABACUS (T. Helgaker, H.J. Aa. Jensen, P. Jrgensen, and J. Olsen), and ECP routines by A. V. Mitin and C. van Wllen. For the current version, see http://www.cfour.de.

[57] K. Kimura, S. Katsumata, Y. Achiba, T. Yamazaki and S. Iwata, *Ionization energies, Ab initio assignments, and valence electronic structure for 200 molecules* in Handbook of HeI Photo-

electron Spectra of Fundamental Organic Compounds, Japan Scientific Soc. Press, Tokyo, 1981.

[58] G. Bieri, F. Burger, E. Heilbroner and J. P. Maier, *Helv. Chim. Acta*, 1977, **60**, 2213.

[59] K. Levenberg, *Quart. Appl. Math.*, 1944, **2**, 164-168

[60] D. W. Marquardt, *SIAM J. Appl. Math.*, 1963, **11**, 431-441.

[61] M. A. Melvin, *Rev. Mod. Phys.*, 1956, **28**, 18.

[62] E. Ascher, *J. Phys. C.*, 1977, **10**, 1365.

[63] P. Murray-Rust, H. -B. Bürgi and J. D. Dunitz, *Acta. Crystallogr., Sect. A*, 1979, **A35**, 703.

[64] E. B. Wilson, Jr., J. C. Decius and P. C. Cross, *Molecular vibrations*; McGraw-Hill, New York, 1955.

[65] W. L. Clinton and B. J. Rice, *J. Chem. Phys.*, 1959, **30**, 542.